CHAPTER 7

Rigid Motion Invariant Classification of 3D Textures and Its Application to Hepatic Tumor Detection

Sanat Upadhyay*, Saurabh Jain†, Manos Papadakis‡
*University of Houston, Computational Biomedicine Lab, Houston, TX, United States
†THINK Surgical Inc., Fremont, CA, United States
‡University of Houston, Houston, TX, United States

Abstract

Soft tissue in 3D medical data sets is often associated with 3D textures. The granularity demonstrated by tissues in medical images due to natural tissue structure gives rise to 3D or 2D textures. In this chapter, we focus on 3D textures for the purpose of classifying tissue patches into healthy and pathological. In our case, both patch types come from the same organ but one is neoplastic. We view the problem of tissue segmentation/classification into pathological and normal as a problem of 3D texture segmentation/identification. Texture segmentation/identification requires two major components, which are often developed together: the representation of the original data and the segmentation/classification algorithm. We model textures as spatial stochastic processes in order to address the variability due to intratissue natural variation, and due to noise. To address this problem, we use isotropic multiresolution analysis to extract 3D rigid motion invariant texture patch signatures. Using a measure of statistical disparity combined with local average intensities, we create low dimensional features that can be used for distinguishing normal tissue patches from pathological ones. We describe how to eliminate the additional variability of 3D tissue texture models due to rigid motions. We also present experimental results on contrast enhanced CT scans of the liver to demonstrate our approach for tissue discrimination, using 3D rigid motion invariant texture classification.

Keywords

Isotropic MultiResolution Analysis (IMRA), Gaussian Markov Random Field (GMRF), Support vector machines, Liver cancer, 3D texture classification, Isotropic filter, Kullback–Leibler divergence, Feature space

7.1 INTRODUCTION

Over the course of the last two decades, a variety of deterministic or stochastic texture models and an even richer ensemble of texture discrimination methods have appeared in the literature, *e.g.*, [1–5]. Texture analysis has extensively been used to build assistive tools for diagnosis; some examples of which can be found in [6–10]. Additional work in this area can be found in Chapters 1 and 12 of this book. Our list is by no means exhaustive, but only indicative, restricted to some of the better known reviews of and

contributions in this modern line of research in pattern recognition. However, most of this work is exclusively devoted to 2D textures. These have been extensively used in medical image analysis and the development of diagnostic semantics in X-ray Computed Tomography (CT) and Magnetic Resonance Imaging (MRI) images. Although these image modalities produce 3D images of the human body, still radiologists and assistive analysis software work in 2D on a slice-by-slice basis and then the expert's brain tries to piece everything together in 3D, using prior knowledge of human anatomy and intuition. But could this process be carried out automatically? Tissues grow and live in 3D, and when they develop they do not necessarily pick orientations convenient to imaging analysis tools. This inconvenient truth motivates the use of genuine 3D texture analysis for developing tools for the semi or fully automated analysis of 3D X-ray CT or MRI images. Specializing in X-ray CT, hard tissue like bones are easily detectable and segmentable [11,12]. On the antipodal end, soft tissues are harder to distinguish due to the reduced variability of X-ray scattering properties of soft tissues. This practically eliminates boundaries between such tissues and organs. While organ boundaries can be identified using prior anatomy knowledge, distinguishing healthy from pathological tissue within the same organ is quite challenging in X-ray CT, due to the lack of variation of scattering properties between soft tissues. This is not the case with MRI, where small variations of water density result in observable variations of image intensity. Since both modalities are based on depicting intensities determined by tissue density, a common trick is to use contrast agents, which permeate in various soft tissues and enhance them by differentiating their density properties. While using them is not a complete solution to all of our CT-related image analysis problems, contrast agents are helpful (see Fig. 7.4), but do not solve all problems, since active lesions may not have distinguishable, hypodense, necrotic cores. Two such examples can be found in Fig. 7.4, top left and bottom right panels. This is because average local image intensities change in relation to neighboring tissues, and the permeation of the contrast agent, or lack thereof, generates patterns in 2D or in 3D enabling the segregation of pathologically suspicious from the healthy tissues. These patterns often exhibit large variability, and are harder for an expert's brain to pick than might be for an imaging algorithm to sense, particularly in 3D. A possible distinguishing pattern is the presence of a texture, which is the result of the spatial organization of the tissue and the contrast agent molecules in 2D or 3D patches. One of the challenges is that many of those textures are not structural, in the sense that they do not consist of periodically occurring patterns (see Section 1.2 of Chapter 1). Nevertheless, these patterns may exhibit statistical stability and be represented by stochastic textures. In particular, we model textures with stationary stochastic processes on a discrete lattice. Their structure is not deterministic, which our brains can immediately identify in 2D, but is governed by an unknown probability distribution that we typically do not even attempt to determine, *e.g.*, Gibbs random fields [13]. Natural

local tissue variations modify 3D textures of the same tissue type; in addition, image acquisition "noise" adds another layer of variability to tissue textures.

The problem presented to us is to determine if two tissue samples (patches) are the same or not. To solve this problem, we do not need to know the underlying probability distributions of the stochastic textures associated with the different tissues. All we need is that pathological tissues are distinguishable from normal ones based on the statistical disparity of different probability models associated with each one of them. In other words, we are not looking for a generative model but a discriminative one. To this end, we need to develop quantities that can be computed from the imaging data, which if all are taken into account concurrently, can identify the disparity between the two probability models. This is pretty much what we do in hypothesis testing, where the quantity we use is called a statistic. In our work, we use a vector of random variables as *features*, which live in a multidimensional space, called the *feature space*. We hypothesize that a low dimensional feature space can be used to discriminate between textures. Following our belief, we pursue to determine these features and the metric of their statistical disparity for a given imaging application. We want to develop features suitable for discrimination of soft tissues, which may be positioned in any orientation. Therefore, feature extraction must be insensitive to all possible 3D orientations and the positioning of the tissue patch. This is precisely the motivation for the development of the theory and algorithms we present in this chapter. We also recommend Section 1.3.3 of Chapter 1 and Section 2.4 of Chapter 2 to the reader for a complementary treatise of this topic in 2D. Using a more formal language, we will present a number of theoretical methods and algorithmic tools for 3D rigid motion invariant soft-tissue discrimination. These methods work with the native 3D data instead of a slice-by-slice analysis of the 2D CT slices. We will discuss the challenges of this problem and the practical limitations of various solutions. The presentation herein, unifies our work in [14], [15], and [16] along with some more recent unpublished work.

Our work uses three main tools:

1. The Isotropic MultiResolution Analysis (IMRA) filters to generate projections of tomographic images at various scales.
2. A first-order Gaussian Markov Random Field (GMRF) model, which we fit to each of the images obtained via the multiscale decomposition algorithm induced by the IMRA.
3. Finally, using the fitted multiscale model we define a rotationally invariant statistical disparity distance measure which, due to the use of the IMRA decomposition algorithm, is 3D rigid motion invariant. In practice, we achieve this invariance only approximately using the proposed statistical disparity distance measure.

Combining the rotationally invariant distance between textures at different scales along with difference in mean intensities, we design low dimensional features for classifying different soft tissue types.

In summary, our contributions are the following:

1. A novel rotationally invariant distance between the high dimensional signatures of two arbitrary 3D textures **X** and **Y**; this distance is rigorously based on calculating the Haar integral (with respect to the measure of the 3D rotation group $SO(3)$) of the Kullback–Leibler divergences between pairs of GMRF models associated to each 3D rotation of textures **X** and **Y**.

2. IMRA-based implementation of 3D rotations of tissue patches in a computationally efficient manner, enabling discrimination between stochastic 3D textures having a broad variety of directional characteristics. We will also present the implementation of approximate rotations of image patches using filters with finite length.

3. Rules for the 3D rigid motion invariant texture discrimination and binary classification which take into account the proposed 3D rigid motion invariant distance between textures computed *at a range of scales*. These rules allow the use of simple GMRF models and avoid computationally costly parameter estimation of GMRFs with long range interactions. We experimentally establish that these rules enhance the sensitivity of 3D rigid motion invariant discrimination between 3D textures, and that they are applicable even to non-GMRF textures.

The early detection of liver cancer lesions can potentially improve the management of various forms of liver cancer. Typically, liver lesions are identified using contrast enhanced CT scans acquired at different phases of perfusion of the hepatic parenchyma by the infused contrast agent. The task of identifying the lesions is performed by a radiologist using a large number of images generated from this multiphase CT acquisition, and requires significant time and effort.

In this work, we present an algorithm and experimental results that demonstrate the feasibility of the development of a semiautomatic screening tool capable of detecting liver abnormalities in contrast enhanced X-ray CT-scans. Specifically, utilizing ideas proposed by Jain et al. [16], we develop 3D rigid motion invariant texture features. We experimentally establish that when these features are combined with mean attenuation intensity differences the new augmented features are capable of discriminating normal from abnormal liver tissue in arterial phase contrast enhanced X-ray CT-scans with high sensitivity and specificity.

When scans are acquired during different perfusion phases of the contrast agent, liver lesions result in hypodense or hyperdense Regions Of Interest (ROI) relative to normal hepatic parenchyma. Quite often, in the arterial phase hypodense ROIs are adjacent to denser ones. These denser regions may be hyperdense due to the increased vascularization of active cancerous lesions, or just normal parenchyma. More specifically, the driving assumption in our approach is that liver tissue ROIs can be represented in a contrast-enhanced X-ray CT scan by two components, *3D texture* and *local mean intensities*. The first of these two components captures the structure, while the second provides the average intensity of the ROI, which is a traditional feature for tissue discrimination.

Local attenuation intensity averages alone are not robust enough to discriminate normal from pathological tissue within the same organ [15].

Past literature has been mostly focused on 2D textures and has introduced a great variety of texture features ranging, for instance, from spatial frequencies based on Gabor filters [17–21] and wavelets [22–27] to autoregressive models such as Markov random fields [28–33]. For 2D texture characterization by local texture information linked to multipixel statistics, spatial interaction stochastic models such as Gibbs random fields have been widely studied [34,35,13]. In particular, Gaussian Markov Random Fields (GMRF) have been extensively applied for 2D texture classification [29,17,36,1], and more recently for 3D textures in [37]. Existing literature on 3D texture models and discrimination is still limited due to serious computational challenges native to 3D image analysis (see [38–42]).

Texture-based lesion segmentation has been successfully used in the past for the detection of cancerous hepatic lesions [43]. Texture features have been extracted in a slice-by-slice manner by combining first- and second-order moments [44]. Very similar approaches have also been used to segment the liver from neighboring organs [45–47]. Apart from the fact that our methods are natively designed to work in 3D, a fundamental difference between previous texture-based approaches and our work is that they use significantly more complex classifiers. Liver segmentation and detection of cancerous lesions has mostly been performed with nontexture based methods as in [48–53], where the difference in attenuation intensity between more and less contrast-perfused ROIs is used for traditional attenuation-based feature extraction, or as in [54,55], where deformable models are utilized to generate the boundaries between normal and abnormal tissues. Both of these approaches mostly limit the detection of cancer lesions to the hypo/hyperdense regions, because differences in average intensities are typically one of the dominant discriminative features. On the other hand, texture and local intensity average based features improve the discriminability between hypodense, hyperdense ROIs, and normal parenchyma, small or big lesions. If in addition, of 3D rigid motion invariance, or covariance is added to the generation of these features, then their robustness will be increased. Another interesting discussion on this topic is presented in Section 2.4.4 of Chapter 2, where directionally sensitive and insensitive features are compared. Before proceeding, we need to clarify that although our feature extraction utilizes isotropic filters, the features we extract have directionality. The isotropy of our filters helps to make our features, at least in their mathematical formulation, 3D rigid motion invariant.

Despite numerous notable successes in the field of hepatic tumor detection and segmentation, our work opens an unexplored direction. The proposed 3D rigid motion invariant features allow feature vectors from normal tissue samples to form clusters that are better defined than the clusters formed when the 3D texture features do not account for 3D rotations. This enhances the discriminatory power of the proposed fea-

tures (Fig. 7.5). Our experimental results are not directly comparable with the results of others, because we only test the discriminative power of our features on sets of ROIs and we do not segment normal from abnormal liver tissue. However, it appears that the proposed features can be used for tissue discrimination with high sensitivity and specificity rates rendering them as a promising tool for developing segmentation algorithms. In Section 7.2, we present the fundamentals of Isotropic MultiResolution Analysis (IMRA) along with some of its theoretical highlights. IMRA is a multiresolution analysis ([56]) modified to be compatible with local rotations of an image patch. For the sake of the audience of this volume, a more detailed discussion on the how IMRA becomes compatible with local rotations is included in Section 7.2. In Section 7.4, we present the basic concepts of our approach and the ingredients of the algorithmic implementation of the proposed 3D rigid motion invariant texture distance. Section 7.5 discusses the use of this distance for multiscale 3D rigid motion invariant texture discrimination/classification, and includes a summary of the algorithmic implementation of our method. We briefly describe our experimental results in the Conclusions section.

7.2 ISOTROPIC MULTIRESOLUTION ANALYSIS

Isotropic MultiResolution Analysis (IMRA) [57] is an MRA for which the "core" subspace V_0 is invariant under rotations. An MRA is collection of closed subspaces of $L_2(\mathbb{R}^D)$ satisfying properties 1–4 of Definition 7.1. MRAs were introduced by Mallat and Meyer in the early 1980s as an attempt to formalize the connection between the analog and digital domains at various levels of resolution and provide a rigorous theoretical justification of the correspondence between mathematical operations applied on images in the physical domain and digital manipulations of their digital counterparts using filter banks. The introduction of MRA sparked an enormous amount of work both in the domain of pure mathematical analysis as well as in algorithmics and engineering applications.

The Fourier transform $\widehat{f} : \mathbb{R}^D \longrightarrow \mathbb{C}$ of $f \in L_1(\mathbb{R}^D)$ is defined by

$$\forall \boldsymbol{\omega} \in \mathbb{R}^D, \ \widehat{f}(\boldsymbol{\omega}) = \int_{\mathbb{R}^D} f(\boldsymbol{x}) e^{-2\pi i <\boldsymbol{x}, \boldsymbol{\omega}>} d\boldsymbol{x}.$$

Here, $L_p(\mathbb{R}^D)$, where $1 \leq p < \infty$, denotes the space of functions defined on the continuous domain $\mathbb{R}^D$ for which

$$\int_{\mathbb{R}^D} |f(\boldsymbol{x})|^p d\boldsymbol{x} < \infty,$$

$<\boldsymbol{x}, \boldsymbol{\omega}>$ denotes the standard inner product on $\mathbb{R}^D \times \mathbb{R}^D$. The map $f \rightarrow \widehat{f}$ restricted to $L_1(\mathbb{R}^D) \cap L_2(\mathbb{R}^D)$ extends to a unitary map on $L_2(\mathbb{R}^D)$. Further down in this section, the

reader will encounter $\mathbb{T}$ which denotes the interval $[-\frac{1}{2}, \frac{1}{2}]$, the fundamental domain of all 1-periodic functions. So, if $f \in L^p(\mathbb{T}^D)$, then f is a periodic function extended to the entire $\mathbb{R}^D$, but p-integrable inside $\mathbb{T}^D$ only.

A *frame* for a separable Hilbert space H is a sequence $\{f_i\}_{i\in\mathbb{I}} \subseteq H$, where $\mathbb{I}$ is a countable index set, for which there are constants $c_0, c_1 > 0$ such that

$$\forall f \in H, \ c_0 ||f||^2 \leq \sum_{i\in\mathbb{I}} |\langle f, f_i \rangle|^2 \leq c_1 \left\| f \right\|^2 .$$

c_0 and c_1 are called frame constants. The weaker version of the above inequality where $c_1 > 0$ such that the right-hand side of the above inequality is valid for all $f \in H$ is termed by referring to $\{f_i\}_{i\in\mathbb{I}}$ as a *Bessel* sequence. If $c_0 = c_1$, we say the frame is *tight*, and a tight frame with $c_0 = c_1 = 1$ is called a *Parseval* frame. A frame is a Riesz basis for H if it is also a minimal family generating H. We use the terms frame (Riesz) sequence when we refer to a countable frame or a Riesz basis of a subspace of a Hilbert space. For $\boldsymbol{x} \in \mathbb{R}^D$ and $r > 0$, $B(\boldsymbol{x}, r)$ will denote the ball centered at $\boldsymbol{x}$ with radius r. By $\mathrm{supp} f$ we mean the set of points $\boldsymbol{x}$ such that $f(\boldsymbol{x}) \neq 0$ and $e_{\mathbf{n}}(\boldsymbol{\omega}) := e^{-2\pi i <\mathbf{n}, \boldsymbol{\omega}>}$, with $\boldsymbol{\omega} \in \mathbb{R}^D$. We define the unitary rotation operator by $\mathcal{R}_{\mathbf{A}}f(\boldsymbol{x}) := f(\mathbf{A}^T \boldsymbol{x})$, where $f \in L_2(\mathbb{R}^D)$, $\boldsymbol{x} \in \mathbb{R}^D$, $\mathbf{A} \in SO(D)$ and $\mathbf{A}^T$ denotes the transpose of the matrix $\mathbf{A}$. We also define a translation by $\boldsymbol{\gamma} \in \mathbb{R}^D$ via $T_{\boldsymbol{\gamma}}f(\boldsymbol{x}) = f(\boldsymbol{x} - \boldsymbol{\gamma})$ for all $\boldsymbol{x}$.

Given $\Omega \subset \mathbb{R}^D$ with positive measure, PW_Ω is the closed subspace of $L_2(\mathbb{R}^D)$ defined as

$$PW_\Omega = \{f \in L_2(\mathbb{R}^D) : \ \mathrm{supp}\widehat{f} \subseteq \Omega\}.$$

The subspace PW_Ω is called a *Paley–Wiener* subspace of $L_2(\mathbb{R}^D)$ associated to Ω. In the special case when Ω is a ball of radius r centered at the origin $\mathbf{0}$, we denote the associated *Paley–Wiener* subspace of $L_2(\mathbb{R}^D)$ by PW_r.

One of the major achievements of the MRA theory is the extension of Shannon's sampling theorem for band-limited functions, which bridges mathematically the digital and analog domains. The interested reader, who wishes to dig a bit more may find that in Property 4 of Definition 7.1 we do not mention anything about the generators of the core subspace V_0. This is not a mistake. It can be proved that there is always a set of functions φ_i whose integer translates $T_{\mathbf{n}}$ generate V_0. The most used cases of MRA are those who are generated by a single function φ, often called scaling function or father wavelet. The MRA theory allows the easy construction of wavelets, which became quite popular in the 1980s and 1990s. One of major discussion items in MRA theory is its invariance to 2D–3D rigid motions. This problem turns out to be subtle. As we see from Property 4 of Definition 7.1, MRA-core subspaces are invariant only by integer translates. The only core subspaces which can be invariant to all translates are the Paley–Wiener ones, but those suffer from the fact that the induced filter banks are implemented by filters with infinite length and significant oscillations. Such filters are

not nice for applications, especially for texture analysis. One way to fix this problem is to smooth their Fourier transforms (Fig. 7.2B shows the Fourier transform of such a filter). The length of the filter will still be infinite but the oscillations will almost go away (Fig. 7.2A). Then the filter can be truncated in order to be used. Or one can choose to implement the filter with fast convolution via the Fast Fourier Transform (FFT), which is what we do here. Then we retain the property of translation invariance of V_0. This implies that if $f \in V_0$ then $T_{\mathbf{y}}f \in V_0$. This allows to recalculate the coefficients of the expansion of $T_{\mathbf{y}}f$ with respect to the $T_{\mathbf{n}}\varphi$'s, using only the coefficients of the expansion of f with respect to the $T_{\mathbf{n}}\varphi$'s. This is precisely what we refer to as translation covariance of V_0. This property is inherited to every V_j. General MRAs have only translation covariance, to translate only by dyadic rational increments. Using the dilation operator, we can move a dilation of f in V_j in which we can calculate the coefficients of the dyadic rational translation of f: Take $f \in V_0$ and let $f = \sum_{\mathbf{n}} c_{\mathbf{n}} T_{\mathbf{n}}\varphi$. Then

$$T_{2^{-j}\mathbf{n}_0}f = \sum_{\mathbf{n}} c_{\mathbf{n}} T_{2^{-j}\mathbf{n}_0} T_{\mathbf{n}}\varphi. \tag{7.1}$$

Now, the refinability of φ implies

$$\varphi = \sum_{\mathbf{k}} d_{\mathbf{k}} T_{2^{-j}\mathbf{k}}(\varphi(2^j \cdot)) \tag{7.2}$$

which, together with (7.1), imply

$$T_{2^{-j}\mathbf{n}_0}f = \sum_{\mathbf{k}} \left(\sum_{\mathbf{n}} c_{\mathbf{n}} d_{\mathbf{k}-\mathbf{n}_0} \right) T_{2^{-j}\mathbf{k}}(\varphi(2^j \cdot)). \tag{7.3}$$

The key for deriving Eq. (7.3) is that a translate of φ retains the shape of φ and $T_{2^{-j}\mathbf{n}_0}(\varphi(2^j \cdot))$ is one of the generators of V_j, thus allowing to derive an easy, intuitive formula for expressing $T_{2^{-j}\mathbf{n}_0}(\varphi(2^j \cdot))$ in terms of $T_{2^{-j}\mathbf{k}}(\varphi(2^j \cdot))$. The best thing about the previous calculation is that it is exact. In conclusion, there are several ways to facilitate translation covariance in 2D or 3D and any D, with the simplest one being to stick with dyadic rational increments.

On the other hand, the situation is subtle when dealing even with simple rotations, other than those which are multiples of 90°. One of the reasons is that, even if rotations are multiples of 90°, a rotation of φ cannot be expressed in terms of the translates $T_{2^{-j}\mathbf{k}}(\varphi(2^j \cdot))$, unless φ remains invariant under rotations. This is one of the reasons that led us to adopt the IMRA approach and the isotropic refinable functions. The other reason is that a rotation of the sampling grid leaves it invariant only if the rotation is a multiple of 90° (see Fig. 7.1). The latter issue does not pose a challenge, as well as a rotation of φ remains inside V_0 (inspect Figs. 7.2B and 7.2A to get a feeling why this is
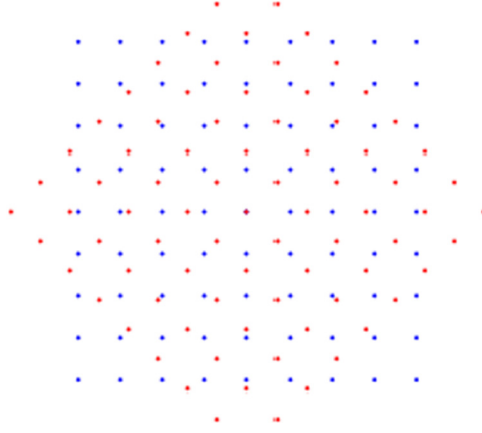
Figure 7.1 Blue dots are the points of the sampling lattice $\mathbb{Z}^2$ and the red dots are the points of this lattice rotated by $45°$. Notice that the red dots almost never come close to the blue ones. (For interpretation of the references to color in this figure legend, the reader is referred to the web version of this chapter.)
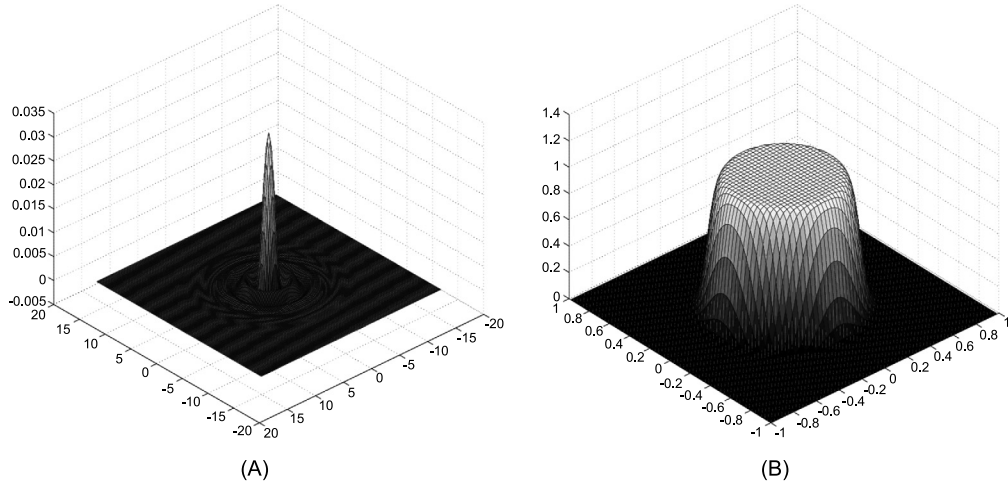
Figure 7.2 A representation of low-pass IMRA filter in (A) space domain (h_0) and (B) frequency domain ($\hat{h}_0$).

true), because then it can be expressed by its translates, pretty much in the same way as we did in Eq. (7.2).

Let Ω be a measurable subset of $\mathbb{R}^D$.

1. We say that $\Omega \subset \mathbb{R}^D$ is *radial* if for all $\mathbf{A} \in SO(D)$, $\mathbf{A}(\Omega) = \Omega$.

2. A $D \times D$ matrix is *expansive* if it has integer entries and if all of its eigenvalues have absolute value greater than 1.

3. An expansive matrix, $\mathbf{A}$, is *radially expansive* if $\mathbf{A}$ is a multiple of a rotation.

Definition 7.1. An Isotropic MultiResolution Analysis (IMRA) of $L_2(\mathbb{R}^D)$ with respect to a radially expansive matrix $\mathbf{A}$ is a sequence $\{V_j\}_{j\in\mathbb{Z}}$ of closed subspaces of $L_2(\mathbb{R}^D)$ satisfying the following conditions:

1. $\forall j \in \mathbb{Z},\ V_j \subset V_{j+1}$,
2. $f \in V_j$, if and only $f(2^{-j}\cdot) \in V_0$ for every $j \in \mathbb{Z}$ (dyadic dilations),
3. $\cup_{j\in\mathbb{Z}} V_j$ is dense in $L_2(\mathbb{R}^D)$ and $\cap_{j\in\mathbb{Z}} V_j = \{0\}$,
4. V_0 is invariant under the action of the group $\{T_{\mathbf{n}} : \mathbf{n} \in \mathbb{Z}^D\}$,
5. If P_0 is the orthogonal projection onto V_0, then

$$\mathcal{R}_{\mathbf{A}} P_0 = P_0 \mathcal{R}_{\mathbf{A}} \qquad \text{for all } \mathbf{A} \in SO(D). \tag{7.4}$$

First, this structure is not a multiresolution analysis in the classical sense, because the existence of an orthonormal or Riesz basis for its "core" subspace V_0 is not required. The problem that concerns wavelet practitioners is the covariance of wavelet representations of images, and signals in general, under shifts or other transformations of the coordinate system. Specializing this problem to images, it is crucial for a significant number of tasks in image analysis to have covariant representations with respect to rigid motions, *i.e.*, rotations and translations of an image especially in two or three dimensions. Such representations are also known as *steerable* and there are previous attempts with directional representations to address this problem in the context of digital images for finite subgroups of the rotation group and in two dimensions [58–70]. Those constructs are not MRA-based and they typically refer to steerability without attempting to define it. To the best of our knowledge, 3D rigid motion covariant multiscale representations are not as widely utilized (see Section 1.3.3 of Chapter 1). At this point, we wish to mention that Section 2.4.3 of Chapter 2 offers an excellent and inspiring motivation and references to representations for texture analysis. In the same chapter, there are also numerous publications on the topic of steerable multidimensional representations including more modern approaches such as Convolutional Neural Networks (CNN).

Specializing on MRAs, it is natural to impose weaker conditions on the MRA subspaces and in particular on the core subspace V_0 for MRAs defined with respect to dilations given by radially expansive matrices before even attempting to construct MRA-wavelet decompositions that are covariant with respect to rigid motions. In our first design, we used radial ideal filters in order to achieve a high degree of symmetry in wavelet filter design [71], generalizing thus the Shannon MRA (for a definition see [72]) in multidimensions. In order to achieve radiality, we relaxed the classical Riesz basis of the integral translates of the scaling function assumption to allow for this set to be a nonminimal frame. All these ideas led us to the addition of the last property in Definition 7.1. The proofs of all results in this section can be found in [57].

Theorem 7.1. *([57]) Let V be an invariant subspace of $L_2(\mathbb{R}^D)$ under the action of the translation group induced by $\mathbb{Z}^D$. Then V remains invariant under all rotations if and only if $V = PW_\Omega$ for some radial measurable subset Ω of $\mathbb{R}^D$.*

As an immediate consequence, we obtain a characterization of IMRAs generated by a single function, in the sense that there exists a function φ such that V_0 is the closed linear span of $\{T^\mathbf{n}\varphi : \mathbf{n} \in \mathbb{Z}^D\}$.

Proposition 7.1. *([57]) Let $\mathbf{A}$ be a radially expansive matrix and $\mathbf{C} := \mathbf{A}^*$, the transpose of $\mathbf{A}$. A sequence $\{V_j\}_{j\in\mathbb{Z}}$ is an IMRA with respect to $\mathbf{A}$ if and only if $V_j = PW_{\mathbf{C}^j(\Omega)}$, where Ω is radial and satisfies:*

  (i) $\Omega \subset \mathbf{C}(\Omega)$.
 (ii) The set-theoretic complement of $\cup_{j=1}^\infty \mathbf{C}^j(\Omega)$ is null.
(iii) $\lim_{j\to\infty} |\mathbf{C}^{-j}(\Omega)| = 0$.
Moreover, the only singly generated IMRAs are precisely $V_j = PW_{\mathbf{C}^j(\Omega)}$, where (Ω) is a radial subset of $\mathbb{T}^D$ satisfying (i), (ii), and (iii).

The previous result has more theoretical than practical value. MRAs play a significant role in the theory because they model the transition from analog to digital and backward. However, for practical purposes, it will be desirable to work with a single generator function of an MRA. The nesting of the subspaces V_j forces us to choose such a function to be refinable: A function φ in $L_2(\mathbb{R}^D)$ is called *refinable*, with respect to dilations induced by an expansive matrix $\mathbf{A}$, if there exists a measurable, essentially bounded, $\mathbb{Z}^D$-periodic function $\widehat{h}_0$ such that $\widehat{\varphi}(\mathbf{A}^*\boldsymbol{\omega}) = \widehat{h}_0(\boldsymbol{\omega})\widehat{\varphi}(\boldsymbol{\omega})$, a.e. $\boldsymbol{\omega} \in \mathbb{R}^D$. The function $\widehat{h}_0$ is called the low–pass filter or mask corresponding to φ, which also plays the role of the sampling kernel. Scaling functions are refinable. The latter property assumption can be formalized by requiring $\{T^\mathbf{n}\varphi : \mathbf{n} \in \mathbb{Z}^D\}$ to be a Bessel family. When φ satisfies this property and it is refinable, then it is a scaling function.

A naturally arising question is which are the refinable functions φ that give rise to IMRAs. An obvious choice is a function whose Fourier transform is the characteristic function of set Ω described in the previous proposition, whose discontinuities destroy its spatial localization. The characterization of isotropic refinable functions is nontrivial and it is thoroughly studied in [57]. Here, we include only two relevant results indicating that such functions are not the most desirable for applications.

Theorem 7.2. *([57]) Let $\mathbf{A}$ be a radially expansive matrix and $\varphi \in L_2(\mathbb{R}^D)$ be a refinable function with mask $\widehat{h}_0 \in L_\infty(\mathbb{T}^D)$. If φ is isotropic (Fig. 7.2B), then it is not compactly supported in the spatial domain. Moreover, an IMRAs cannot be defined by φ, if $\hat{\varphi}$ does not vanish outside the ball of radius $1/2$.*

The previous theorem dictates, in order to have full 3D rigid motion steerability in a MRA setting we must work with functions which are band-limited within the ball

$B(\mathbf{0}, 1/2)$ in the frequency domain if we want to work with dyadic dilations. Translation invariance can be achieved by avoiding downsampling at every decomposition level. However, the lack of natively finite length filters for IMRA implementations imposes the need to truncate isotropic low and high pass filters and in some applications this may be a problem. In Section 7.3, we will suggest a method on how to partially overcome this problem by settling for a concept of rotational steerability limited to some finite orientations. There is another aspect of the IMRA that we need to elaborate on before wrapping up this section. Isotropy may be viewed as potentially losing sensitivity to directional characteristics of an image. This is actually not true. The autocovariance function of the probability model we will use for texture feature extraction is primarily a model of three fundamental directions of correlation. The IMRA does not smooth out those directionalities or wave front orientations. On the contrary, it preserves them. Its subbands show the same sensitivity regardless of the orientation of a singularity or of the directions in which the correlations appear to be stronger or weaker. What the IMRA misses is the ability to identify these directions, because its subbands depend only on scale and they are rotationally invariant.

7.3 IMPLEMENTING ROTATIONS WITH COMPACTLY SUPPORTED REFINABLE FUNCTIONS

The conclusion, Theorem 7.2, of the previous section naturally leads to consider MRA structures where the core subspace invariance under rotations. In fact, one of the big problems is that the rotation of a refinable function is no longer refinable. This is because rotations do not preserve the integer sampling grid (Fig. 7.1), so $\hat{h}_0(\mathbf{A}\cdot)$, the low pass filter corresponding to $\varphi(\mathbf{A}\cdot)$, the rotation of a refinable φ by $\mathbf{A}$, is not necessarily a periodic function. But why should we care about refinable functions? The reason is that those functions allow the use of filter banks for implementing fast multiscale decompositions of images. Our attempt to circumvent this particular problem is to abandon classical rotations and instead use orthogonal matrices with integer entries. As we later on argue, this trick will help to use compactly supported refinable functions and implement "approximate rotations" of them. But why should we care about this class of refinable functions? The answer is they lead to MRAs implementable with convolutional finite length filter. This prevents ringing, approximation numerical errors, and distant correlations which infinite length filters, even truncated, suffer from. For clarity purposes, our discussion is restricted to two dimensions, but all arguments can be easily extended to 3D. To simplify the notation, we also use only dyadic dilations.

Consider $\mathbf{A}_i = \begin{pmatrix} a_i & -b_i \\ b_i & a_i \end{pmatrix}$ with $a_i, b_i \in \mathbb{Z}^+$ and $i = 1, 2, ..., n_0$. The columns of $\mathbf{A}_i$ are orthogonal with norm $\sqrt{a_i^2 + b_i^2}$. Essentially each

$$\mathbf{A}_i = \sqrt{a_i^2 + b_i^2} \begin{pmatrix} \dfrac{a_i}{\sqrt{a_i^2 + b_i^2}} & \dfrac{-b_i}{\sqrt{a_i^2 + b_i^2}} \\ \dfrac{b_i}{\sqrt{a_i^2 + b_i^2}} & \dfrac{a_i}{\sqrt{a_i^2 + b_i^2}} \end{pmatrix}$$

can be thought of as the multiple of a rotation matrix by an angle $\theta = \arctan(b_i/a_i)$.

Suppose $f \in L^2(\mathbb{R}^2)$ is an image such that $\widehat{f}(\boldsymbol{\omega}) = \widehat{\mu}(\boldsymbol{\omega})\widehat{\varphi}(\boldsymbol{\omega})$, where $\widehat{\mu} \in L^2(\mathbb{T}^2)$, and φ is a compactly supported refinable function. Images have finite extent, so $\widehat{\mu}$ is a trigonometric polynomial. In other words, the image f belongs to the zero-scale resolution space defined by the integer translates of φ. We called this space V_0 in the previous section. If we now rotate the image f by $\theta = \arctan(-b_i/a_i)$ and normalize accordingly inside the argument of f, i.e., to take $f(\det(\mathbf{A}_i)^{-1}\mathbf{A}_i^T \cdot)$, we have

$$\widehat{f}(\mathbf{A}_i\boldsymbol{\omega}) = \widehat{\mu}(\mathbf{A}_i\boldsymbol{\omega})\widehat{\varphi}(\mathbf{A}_i\boldsymbol{\omega}) .$$

If $\mathbf{A}_0 = \begin{pmatrix} 2^J & 0 \\ 0 & 2^J \end{pmatrix}$, and we set $\widehat{\varphi}_0(\boldsymbol{\omega}) = \widehat{\varphi}(\mathbf{A}_0\boldsymbol{\omega})$, with $\boldsymbol{\omega} \in \mathbb{R}^2$, then we obtain

$$\widehat{f}(\mathbf{A}_i\boldsymbol{\omega}) = \widehat{\mu}(\mathbf{A}_i\boldsymbol{\omega})\widehat{\varphi}(\mathbf{A}_i\boldsymbol{\omega}) = \widehat{\mu}(\mathbf{A}_i\boldsymbol{\omega})\widehat{\varphi}(\mathbf{A}_0(\mathbf{A}_0^{-1}\mathbf{A}_i\boldsymbol{\omega})) = \widehat{\mu}(\mathbf{A}_i^T\boldsymbol{\omega})\widehat{\varphi}_0(\mathbf{A}_0^{-1}\mathbf{A}_i\boldsymbol{\omega}) \qquad (7.5)$$

where

$$\widehat{\varphi}_0(\mathbf{A}_0^{-1}\mathbf{A}_i\boldsymbol{\omega}) = \widehat{\varphi}(\mathbf{A}_0(\mathbf{A}_0^{-1}\mathbf{A}_i\boldsymbol{\omega})) = \widehat{\varphi}(\mathbf{A}_i\boldsymbol{\omega}).$$

On the other hand, we have $\widehat{f_0}(\boldsymbol{\omega}) = \widehat{f}(\mathbf{A}_0\boldsymbol{\omega}) = \widehat{\mu}(\mathbf{A}_0\boldsymbol{\omega})\widehat{\varphi}_0(\boldsymbol{\omega})$. Then applying the transformation $\boldsymbol{\omega} \longmapsto \mathbf{A}_0^{-1}\mathbf{A}_i\boldsymbol{\omega}$, yields $\widehat{f}(\mathbf{A}_i\boldsymbol{\omega}) = \widehat{f_0}(\mathbf{A}_0^{-1}\mathbf{A}_i\boldsymbol{\omega})$. So,

$$\widehat{f_0}(\mathbf{A}_0^{-1}\mathbf{A}_i\boldsymbol{\omega}) = \widehat{\mu}(\mathbf{A}_i\boldsymbol{\omega})\widehat{\varphi}_0(\mathbf{A}_0^{-1}\mathbf{A}_i\boldsymbol{\omega}), \quad a.e. \qquad (7.6)$$

But

$$\mathbf{A}_0^{-1}\mathbf{A}_i = \frac{1}{2^J}\begin{pmatrix} a_i & -b_i \\ b_i & a_i \end{pmatrix} = \frac{\sqrt{a_i^2 + b_i^2}}{2^J}\begin{pmatrix} \dfrac{a_i}{\sqrt{a_i^2 + b_i^2}} & \dfrac{-b_i}{\sqrt{a_i^2 + b_i^2}} \\ \dfrac{b_i}{\sqrt{a_i^2 + b_i^2}} & \dfrac{a_i}{\sqrt{a_i^2 + b_i^2}} \end{pmatrix}. \qquad (7.7)$$

If we take $(a_i, b_i) \in \mathbb{Z}^+ \times \mathbb{Z}^+$, and J to be such that $\frac{\sqrt{a_i^2 + b_i^2}}{2^J}$ is close to 1, then we have that $\mathbf{A}_0^{-1}\mathbf{A}_i$ is an approximate rotation by $\arctan\left(-\frac{b_i}{a_i}\right)$. Thus Eqs. (7.6) and (7.7) imply that in order to apply the approximate rotation $\mathbf{A}_0\mathbf{A}_i^{-1}$ to f_0, we have to switch to an appropriate scale. In the space domain, this operation amounts to oversampling. As we know, the accurate approximation of 2D curves requires high resolution as anyone who holds this volume with the intent to review it knows. The rotation/scaling $x \to \det(\mathbf{A}_i)^{-1}\mathbf{A}_i^T x$ amounts to changing the scale from the nominal to a coarse one, approximately by 2^{-J} and then implementing an approximate rotation by a certain angle, which will leave the integer sampling grid invariant. Since we do not leave the integer grid, all computations are accurate to the extent that the approximate rotation is satisfactory enough. Moreover, all implementations are with finite length filters (no need for filter truncations).

This method allows us to implement with high accuracy a finite number of rotations of images in 2D and using Euler angles even in 3D. What we have shown so far is that the approximate rotation (given that this statement $\frac{\sqrt{a_i^2 + b_i^2}}{2^J}$ is close to 1 is satisfactory for the time being), of f_0 by $\arctan\left(-\frac{b_i}{a_i}\right)$ can be computed with precise operations in the discrete domain. Therefore to implement approximately rotations by $\arctan\left(-\frac{b_i}{a_i}\right)$, $i = 1, 2, ..., n_0$, we need to select (a_i, b_i) in such a way that $\frac{\sqrt{a_i^2 + b_i^2}}{2^J}$, where J is fixed suitable scale, is close to 1. Finally, we must mention that, in practice, we work with the samples of f interlaced by J zeros per dimension. Of course, this causes aliasing and in order to remove this aliasing we need to reverse to extreme oversampling by low passing and by downsampling J times. The opposite of this procedure will be used in the next section when rotations will be implemented approximately using the nonfinite IMRA filters.

7.4 CONNECTING IMRA WITH STOCHASTIC TEXTURE MODELS USING GAUSSIAN MARKOV RANDOM FIELDS (GMRF)

Stochastic textures are often modeled by random fields. A *random field* $\mathbf{X} = \{X_s : s \in S\}$ is a set of real–valued random variables defined on the same probability space. Such a field is called *Gaussian* if any finite linear combination of the $\{X_s\}$ has a Gaussian distribution. A first step in texture discrimination or classification is to define a *texture signature*, specified as a vector of computable texture features, belonging to a fixed finite or infinite dimensional Feature Vector Space (FVS). High dimensionality of FVS formally facilitates texture discrimination by their signatures at the expense of computational cost and higher sensitivity to noise.

We work with 3D textures, which we model as random fields defined on the continuous domain $\mathbb{R}^3$. After image acquisition, realizations of these textures are digital 3D images, where we assume, that image intensities at gray levels are given only for points in a discrete sampling lattice. Nonetheless, our approach easily extends to multicomponent images. Specifically, given an arbitrary, stationary 3D texture $\mathbf{X}$ with zero mean defined on a fixed 3D rectangular lattice $\mathbf{\Lambda} \subset \mathbb{R}^3$ similar to $\mathbb{Z}^3$, we assume that $\mathbf{X}$ is the restriction to $\mathbf{\Lambda}$ of a "continuous parent" 3D texture $\{X_s, \, s \in \mathbb{R}^3\}$ is generated by a stationary Gaussian random field which we will also denote by $\mathbf{X}$ for brevity. The autocovariance function ζ of $\mathbf{X}$ is defined by $\zeta(\boldsymbol{u}) = \mathrm{Cov}(X_s, X_{s+\boldsymbol{u}})$ for all $\boldsymbol{u}$ and $\boldsymbol{s}$ in $\mathbb{R}^3$ and we assume that it satisfies the following properties:

1. The Fourier transform of ζ is C^∞.

2. The support of $\widehat{\zeta}$, is contained in a ball centered at the origin.

The second property above is used to place ζ in a IMRA subspace. The first property imposes a natural property for ζ, the rapid decay in space, which prevents correlations between distant voxels.

The $\mathbf{A}$-rotation of a continuous 3D texture $\mathbf{X}$, denoted by $\mathbf{X}^{\mathbf{A}}$ is the continuous texture such that the random variable $(X^{\mathbf{A}})_s$ corresponds to the random variable $X_{\mathbf{A}^T s}$. Obviously, the "continuous" parent texture is not affected by 3D rigid motions. While 3D translates induced by the action of $\mathbb{Z}^3$ do not affect the discrete texture $\mathbf{X}$, due to the spatial homogeneity assumption, the discrete texture $\mathbf{X}$ is not invariant under random 3D rotations, in general. Hence, for each 3D rotation $\mathbf{A} \in SO(3)$, $\mathbf{X}^{\mathbf{A}}$ is defined by first applying the rotation $\mathbf{A}$ to the continuous "parent" texture $\mathbf{X}$, and then by restricting this rotated continuous texture to $\mathbf{\Lambda}$.

Let $b_0 > 0$ be the radius of the ball in Item 2 above and $0 < b < 1/2$ satisfies $2^{j-1}b < b_0 < 2^j b$ for some scale $j \in \mathbb{Z}^+$. We use an IMRA $\{V_j\}_j$ generated by a radial refinable function φ with C^∞ Fourier transform $\widehat{\varphi}$ such that $\widehat{\varphi}(\boldsymbol{\omega}) = 1$ for all $|\boldsymbol{\omega}| \leq 2^{-j}b_0$ and $\widehat{\varphi}(\boldsymbol{\omega}) = 0$ for $|\boldsymbol{\omega}| \geq b$. Then V_0 contains all L_2-functions whose Fourier transform is supported in the ball of radius b, therefore $\zeta \in V_j$. With no loss of generality, we may and will always assume $j = 0$, so that $b/2 < b_0 < b$. Hence $\widehat{\varphi} = 1$ on the support of $\widehat{\zeta}$, which implies that for all $\boldsymbol{k} \in \mathbb{Z}^3$, $\langle \zeta, T_{\boldsymbol{k}}\varphi \rangle = \zeta(\boldsymbol{k}) = Cov(X_{\boldsymbol{k}}, X_{\mathbf{0}})$.

The properties of ζ imply that the autocovariance $\zeta_{\mathbf{A}}$ of the continuous texture $\mathbf{X}^{\mathbf{A}}$ is given by $\zeta_{\mathbf{A}} = \mathcal{R}_{\mathbf{A}}\zeta$. Our goal is to calculate the autocovariance of the discrete texture $\mathbf{X}^{\mathbf{A}}$ which is the restriction of its continuous counterpart on the lattice $\mathbb{Z}^3$. Equivalently, we want to estimate the sequence $\{\zeta_{\mathbf{A}}(\boldsymbol{k})\}_{\boldsymbol{k} \in \mathbb{Z}^3}$ for all rotations $\mathbf{A}$ from the known input $\{\zeta(\boldsymbol{k})\}_{\boldsymbol{k} \in \mathbb{Z}^3}$. Since $\zeta \in V_0$ we conclude that $\zeta_{\mathbf{A}}$ belongs to V_0 as well, hence $\zeta_{\mathbf{A}}$ is accurately represented by its values $\{\zeta_{\mathbf{A}}(\boldsymbol{k})\}_{\boldsymbol{k} \in \mathbb{Z}^3}$ on the same lattice regardless of the rotation $\mathbf{A}$. Therefore the $\boldsymbol{k}$th value of $\zeta_{\mathbf{A}}$ is given by

$$\zeta_{\mathbf{A}}(\boldsymbol{k}) = \langle \mathcal{R}_{\mathbf{A}}\zeta, T_{\boldsymbol{k}}\varphi \rangle = \langle \zeta, T_{\mathbf{A}\boldsymbol{k}}\mathcal{R}_{\mathbf{A}^T}\varphi \rangle = \langle \zeta, T_{\mathbf{A}\boldsymbol{k}}\varphi \rangle, \qquad \boldsymbol{k} \in \mathbb{Z}^3. \qquad (7.8)$$

Eq. (7.8) is, in fact, a simple steerability rule:

If $\mathbf{A}_1, \mathbf{A}_2$ are two rotations and $(\zeta_{\mathbf{A}_2})_{\mathbf{A}_1}$ is the autocovariance of the rotated texture $\mathbf{X}^{\mathbf{A}_2}$ by $\mathbf{A}_1$, then Eq. (7.8) implies

$$(\zeta_{\mathbf{A}_2})_{\mathbf{A}_1}(\boldsymbol{k}) = \langle \zeta_{\mathbf{A}_2}, T_{\mathbf{A}_1\boldsymbol{k}}\varphi \rangle = \langle \zeta, T_{\mathbf{A}_2\mathbf{A}_1\boldsymbol{k}}\varphi \rangle = \zeta_{\mathbf{A}_2\mathbf{A}_1}(\boldsymbol{k}), \tag{7.9}$$

which shows why Eq. (7.8) is a steerability rule. The computational implementation of this rule is carried out by approximating $\zeta_{\mathbf{A}}(\boldsymbol{k}) = \langle \zeta, T_{\mathbf{A}\boldsymbol{k}}\varphi \rangle$ by $\langle \zeta, T_{2^{-j_0}\boldsymbol{k}'}\varphi \rangle$, where $\boldsymbol{k}' \in \mathbb{Z}^3$, by taking $j_0 > 0$ to be high enough so that points $2^{-j_0}\boldsymbol{k}'$ and $\mathbf{A}\boldsymbol{k}$ are sufficiently close. This computation is performed by iteratively applying j_0-steps of the reconstruction algorithm of the fast IMRA-transform (see Section 7.2).

Discrimination between two generic 3D textures $\mathbf{X}$ and $\mathbf{Y}$ relies on the fitting of multiscale GMRF models after applying arbitrary rotations to $\mathbf{X}$ and $\mathbf{Y}$. Fitting does not require $\mathbf{X}$ or $\mathbf{Y}$ to be Gaussian or stationary. When we fit a statistical model to a texture, we focus on the discriminability of the model, and we ignore that the model we use may not be the actual model of the texture. Hence parameter estimation of GMRFs is used only as a tool to extract local statistically discriminative characteristics of textures. This estimation is part of our feature extraction process. Its discriminability depends on the class of 3D textures that we deal with, and remains to be established with experimental validation. It is quite conceivable that for other types of textures more complex GMRF models may be necessary. The complexity of these parameter estimations increases quickly when one increases the size of the basic neighborhoods defining these Gibbs random fields [73]. Thus to minimize computational costs we deliberately restricted the class of GMRFs considered here to those with order-one neighborhoods. But since such models essentially capture only near correlations, we first implement a multiscale decomposition of each texture $\mathbf{X}$ by a fast IMRA decomposition algorithm and we then fit GMRFs with order-one neighborhoods to each one of these monoscale texture outputs. This multiscale parametrization does capture medium and long distance correlations between voxels. We will skip all the details about GMRF models, because they will only tire the reader of this volume. The reader may refer to [16] for all of these details.

The next step is to define a 3D rigid motion covariant signature for a discrete texture. A natural assumption for textures is that their statistical properties of interest are invariant under translations within a stationary region, which in our case should be interpreted as tissue homogeneity. Therefore the problem of 3D rigid motion invariant texture discrimination reduces to that of 3D rotationally invariant texture discrimination. Rotationally invariant discrimination between textures has been studied mostly in 2D. For instance, in [74] two circularly symmetric autoregressive models are fitted to the 2D texture data, one for the four nearest neighbors, and one for the four diagonal nearest neighbors. Circularly symmetric models with higher order neighborhoods were used in [17], where the L_1-norm of the outputs of circularly symmetric 2D Gabor filters was a key feature. A basic shortcoming of these models is that rotationally

invariant discrimination between textures is achieved by handling nonisotropic textures as if they were isotropic. A mathematically rigorous treatment of isotropic textures can be found in [75]. However, generic textures often exhibit directional characteristics, which isotropic models cannot capture. The setback of these approaches is recognized in [1], where 2D textures are modeled by continuous stationary GMRFs and 2D image texture rotations are generated via a continuous version of the discrete power spectral density defined by the digitized image data. The best rotation angle matching the given unknown texture to each texture from a predefined gallery of textures is estimated by maximizing a likelihood function derived from the continuous power spectral densities. Texture classification is then carried out by comparing model parameters. This approach worked well in 2D, but a 3D version would be computationally extremely expensive, since the likelihood function in [1], is a product of terms evaluated at each node in a 3D lattice. The approach of [76], based on local binary patterns, seems to be the first attempt to build a 3D texture classification scheme robust to 3D rotations.

Our key idea is to define a computable rotationally invariant distance between any pair of adequately defined 3D texture signatures.

If, $\mathbf{X}$ is a discrete texture, we fit a zero mean GMRF $G_\mathbf{X}(\mathbf{A}, j)$ from the class introduced in the previous section, to the rotated textures $\mathbf{X}^\alpha$ at multiple scales j. There is no harm to assume that mean intensities are zero. The texture is created by intensity variations, occurring in a statistically stable manner to form a texture. Later, in our statistical disparity metric between two tissues we take into account local average differences of density values.

Given two discrete 3D textures $\mathbf{X}$ and $\mathbf{Y}$ with zero intensity means our first choice for a texture "distance" at scale j would be the minimum taken over $\mathbf{C} \in SO(3)$ of the Kullback–Leibler (KL)-divergence of the GMRF models of $G_\mathbf{X}(\mathbf{I_3}, j)$ from $G_\mathbf{Y}(\mathbf{C}, j)$, where $\mathbf{I_3}$ is the 3×3 identity matrix. It seems reasonable to think that this model should in principle be able to give the best rotation matching angle between the two textures. If it does so, then $G_\mathbf{X}(\mathbf{A}, j)$ and $G_\mathbf{Y}(\mathbf{CA}, j)$ should appear statistically indistinguishable with $G_\mathbf{X}(\mathbf{I_3}, j)$ from $G_\mathbf{Y}(\mathbf{C}, j)$, respectively, as $\mathbf{A}$ runs throughout $SO(3)$. At least the KL-divergence between the first and second pair should be identical. This may not be true because the GMRF model is fitted and the $\mathbf{X}$ and $\mathbf{Y}$ are discrete textures rotated by rotations, which do not leave the sampling grid $\mathbb{Z}^3$ invariant.

In particular, the heart of the problem is not to classify textures as "same" or "not the same" by finding their best matching angle but to develop a decision function uniquely designating the value "same" or "different" to all possible configurations of their 3D rigid motions. That is to group 3D textures via an equivalence relation: Two textures $\mathbf{X}$ and $\mathbf{Y}$ are considered to be the same if any 3D rigid motion of $\mathbf{X}$ is declared to be the "same" with a 3D rigid motion of $\mathbf{Y}$. These considerations lead us to choose the orbit $\{G_\mathbf{X}(\mathbf{A}, j) : \mathbf{A} \in SO(3)\}$ of the fitted GMRF model of $\mathbf{X}$. Those orbits are covariant to 3D rotations and invariant to 3D translates (recall that downsampling is

suspended in order to maintain invariance with respect to integer translations). Thus the problem that the first choice of texture distance appears to have, is solved if we instead find a "distance" between the orbits $\{G_\mathbf{X}(\mathbf{A}, j) : \mathbf{A} \in SO(3)\}$ and $\{G_\mathbf{Y}(\mathbf{CA}, j) : \mathbf{A} \in SO(3)\}$. The average over $SO(3)$ of the KL-divergences between the orbits for the fitted Gaussian fields $G_\mathbf{X}(\mathbf{A}, j)$ and $G_\mathbf{Y}(\mathbf{A}, j)$ is an obvious choice of such a "distance." In fact, we define as the 3D rigid motion invariant distance between $\mathbf{X}$ and $\mathbf{Y}$ at the scale j we the minimum taken over $\mathbf{C} \in SO(3)$ of the average of the KL-divergences of the orbits of the GMRF models $G_\mathbf{X}(\mathbf{A}, j)$ and $G_\mathbf{Y}(\mathbf{CA}, j)$ as $\mathbf{A}$ traverses $SO(3)$.

The strictly stationary GMRF $\mathbf{X}$ is assumed to have an autocovariance function ζ tending to 0 at infinity, hence $\mathbf{X}$ is ergodic. Thus (see [77, Theorems III.4.2 and 4.4]) for $|\mathbf{\Lambda}|$ large enough, each $\zeta(\mathbf{k})$ can be approximated with sufficient accuracy by the empirical autocovariance $\zeta_0(\mathbf{k})$. To compare pairs of stationary GMRFs, we use the KL-divergence between stochastic processes. The symmetrized KL-divergence of two N-dimensional Gaussian probability distributions G_1 and G_2, with zero mean and invertible covariance matrices Σ_1 and Σ_2, is given by

$$\text{KLdist}(\Sigma_1, \Sigma_2) = \frac{1}{2}\text{Trace}(\Sigma_2^{-1}\Sigma_1 + \Sigma_1^{-1}\Sigma_2 - 2I_{N\times N}). \qquad (7.10)$$

In light of (7.8), we define the *monoscale 3D rigid motion covariant texture signature of the observed texture* $\mathbf{X}$ *at the scale corresponding to the density of the lattice* Λ by $\Gamma_\mathbf{X}(\mathbf{A}) = (\widehat{\Sigma})_\mathbf{A}$, $\mathbf{A} \in SO(3)$, where $(\widehat{\Sigma})_\mathbf{A}$ is the autocovariance matrix of the fitted GMRF model extracted from $\{(\zeta_0)_\mathbf{A}(\mathbf{k})\}_{\mathbf{k}\in\Lambda}$ by computing it from the rotated texture patch of $\mathbf{X^A}$, using the IMRA filters using $\mathbf{k}$ as the center of the rotation. A $\mathbf{A}$-rotation of the discrete texture $\mathbf{X}$ is the restriction of the $\mathbf{A}$-rotation of its continuous parent on Λ. Rotating the discrete texture $\mathbf{X}$ amounts to rotating the autocovariance ζ of its continuous parent. This leads us to propose 3D texture distance:

$$Rdist(\mathbf{X}, \mathbf{Y}) := \min_{\mathbf{C}\in SO(3)} \int_{SO(3)} \text{KLdist}(\Gamma_\mathbf{X}(\mathbf{A}), \Gamma_\mathbf{Y}(\mathbf{CA}))\, d\mathbf{A}. \qquad (7.11)$$

Since empirical autocovariances are only approximations of the true autocovariances and a very simple GMRF model fitted to the rotations of the texture, we assert that the 3D rotational covariance of $\Gamma_\mathbf{X}$ is true only approximately. This implies that the average of the symmetrized KL-divergence between two texture signatures $\Gamma_\mathbf{X}$ and $\Gamma_\mathbf{Y}$ expressed by *Rdist* is only approximately 3D rotationally invariant [16]. The 3D shift invariance of *Rdist* is implicit in the definition of the texture signature, so it is inherited by *Rdist*.

By taking into account the assumed symmetries of the GMRF-model [16], we select a finite 3D grid of points $(\alpha, \beta, \gamma) \in EB = [0, \pi] \times \left[0, \frac{\pi}{2}\right] \times [0, \pi]$ by defining a partition of *EB* into "cubes" having the same Haar measure. This is achieved by defining a grid

Π_N of points $\mathbf{A}_{(i,l,k)} = (\alpha_i, \beta_l, \gamma_k) \in EB$ where

$$
\begin{aligned}
\alpha_i &= \left\{\frac{i\pi}{N}\right\} \quad i = 0, 1, \dots, N-1, \\
\beta_l &= \left\{\arccos\left(1 - \frac{l+0.5}{N}\right)\right\} l = 0, 1, \dots, N-1, \\
\gamma_k &= \left\{\frac{k\pi}{N}\right\} \quad k = 0, 1, \dots, N-1.
\end{aligned}
$$

The discrete values of β start with 0.5 to avoid the unwieldy *gimbal lock* point $\beta_0 = 0$. Using the discrete set of rotations just defined, a computationally implementable version of the distance *Rdist* defined in Eq. (7.11) is given by

$$
\min_{\mathbf{C} \in SO(3)} \frac{1}{N^3} \sum_{i=0}^{N-1} \sum_{l=0}^{N-1} \sum_{k=0}^{N-1} \text{KLdist}\left(\Gamma_{\mathbf{X}}(\mathbf{A}_{(i,l,k)}), \Gamma_{\mathbf{Y}}(\mathbf{C}\mathbf{A}_{(i,l,k)})\right) . \tag{7.12}
$$

Once again the symmetry properties of the fitted GMRF model imply that the numerical minimization in (7.12) can be restricted to $\mathbf{C} \in EB$ [16]. In our experiments, we chose $N = 5$ or $N = 4$ for synthetic data and $N = 5$ or $N = 6$ for the experiments with the X-ray CT-data.

7.5 FEATURE SPACE FOR ROTATIONALLY INVARIANT TEXTURE DISCRIMINATION

To implement the multiscale *Rdist*-based comparison of two textures, we begin with two realizations $\mathbf{x}^{(0)}$ and $\mathbf{y}^{(0)}$ of the arbitrary 3D textures $\mathbf{X}$ and $\mathbf{Y}$ as above. Both $\mathbf{x}^{(0)}$ and $\mathbf{y}^{(0)}$ are given on an initial finite lattice $\mathbf{\Lambda}^{(0)}$. We apply the IMRA-decomposition algorithm [75,78] to $\mathbf{x}^{(0)}$ and $\mathbf{y}^{(0)}$ in order to generate two corresponding multiscale realizations $\mathbf{x}^{(j)}$ and $\mathbf{y}^{(j)}$ defined for each of the coarser scales $j = -1, -2 - 3, -J$. Convolutions with h_0 (the inverse Fourier transform of $\widehat{h}_0$) can again be performed as fast convolution in the frequency domain. In order to maintain $\mathbb{Z}^3$-translation invariance when we apply the IMRA-decomposition algorithm, we skip the downsampling by 2. In this case, for a single application of the decomposition algorithm, the order-1 neighbors at this scale are the order-3 neighbors, *i.e.*, two voxels apart on each of the x, y, z-directions. This alternative allows to collect more data with the convention that $\mathbf{\Lambda}^{(j)}$ is $\mathbf{\Lambda}^{(0)}$ itself reduced by an appropriate boundary so that order-one neighborhoods at each level j are contained in $\mathbf{\Lambda}^{(0)}$.

Subsequently, for $j = 0, -1, -2-3, -J$, we define $Rdist_j(\mathbf{X}, \mathbf{Y}) = Rdist(\mathbf{x}^{(j)}, \mathbf{y}^{(j)})$. The vector of these $J + 1$ rotationally invariant distances $Rdist_j(\mathbf{x}, \mathbf{y})$, where $j = 0, -1, \dots -J$, will be our multiscale 3D texture discrimination tool.

### 7.5.1 Self-distance for 3D textures

Theoretically the self-distance $Rdist_j(\mathbf{X}, \mathbf{X^A})$ of the 3D texture $\mathbf{X}$ from every rotation of itself at scale j must be zero. However, when we compute the distance of a 3D texture from a rotation of itself, we only achieve an approximate minimization in formula (7.12). Furthermore, note that we implement texture rotations via a rotation of their empirical autocovariance function which adds another level of approximation to $Rdist_j(\mathbf{X}, \mathbf{X^A})$. Hence, in practice, "self-distances" are nonzero. Therefore, discrimination between 3D textures must take these nonzero "self-distances" into account as detailed further down.

To estimate the self-distance of a 3D texture in the extensive numerical tests presented below, we generate rotations of $\mathbf{X}^{(j)}$ by 20 randomly selected $\mathbf{A}_k \in SO(3)$ ($k = 1, 2, \ldots, 20$) and define $diam_{\mathbf{X}}(j)$ to be the 80th percentile of the 20 distances $Rdist(\mathbf{X}^{(j)}, (\mathbf{X}^{(j)})^{\mathbf{A}_k})$. The choice of 20 random rotations and of the 80th percentile were reached after numerical testing which showed that these choices provided a reasonably accurate estimate of the self-distance of the texture whose realization is $\mathbf{X}$. In a nutshell, $diam_{\mathbf{X}}(j)$ is a Monte Carlo estimate of the baseline computational errors that will affect the computation of $Rdist_j(\mathbf{X}, \mathbf{Y})$, the computable distance of $\mathbf{X}$ from any other texture whose realization is $\mathbf{Y}$. This interpretation of $diam_{\mathbf{X}}(j)$ is the key to defining discrimination between 3D textures.

7.6 3D TEXTURE-BASED FEATURES

Our tissue classification scheme consists of two levels of classifiers. The design of both levels is traditional. The first level consists of an ensemble of Support Vector Machines (SVM) classifiers, which at the second level decide by majority voting whether a tissue ROI is normal or abnormal. The SVM classifiers use low-dimensional feature vectors whose components express the statistical disparity at one or more scales of the 3D texture corresponding to a given liver tissue ROI for the 3D texture of a normal reference ROI and the difference of average intensities between the two ROIs. To develop these classifiers the human operator selects a small number of reference normal ROIs from an X-ray CT-scan that is examined. The proposed feature design takes into account that a liver consists of soft tissues with varying 3D orientations thus requiring features to be invariant under 3D rotations and translations. In particular, cancer will tend to develop along blood vessels, which themselves appear with a varying degree of 3D orientations. Moreover, malignancies form their vasculature with an even richer orientation variation in 3D. Attenuation intensity local average–based features would automatically be invariant to 3D rigid motions and, therefore, insensitive to the variety of 3D orientations of the patterns formed by tissues of interest, but 3D texture features must be specifically designed to be 3D rigid motion invariant.

We stress that the 3D texture corresponding to a tissue ROI is almost never an order-one GMRF. Yet, we carry out our computations as if it were such a GMRF. We use this computa-
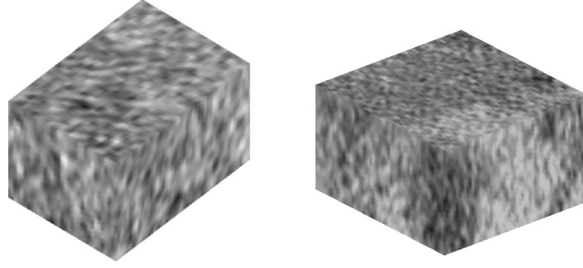
Figure 7.3 Typical 3D view of the texture of a normal liver ROI (left) and of an abnormal (neoplastic) liver ROI (right).

tionally simple and numerically efficient stochastic model as a probe for tissue discrimination and not as a texture model for soft tissues. The 3D texture features for the promised liver tissue SVM classifiers are constructed via (7.11).

Let $\{\mathbf{s}_k\}_{k=1,2,\ldots,N}$ be 3D volumes from normal or abnormal liver tissues and $\mathbf{\Lambda}_k := \mathbf{s}_k \cap \mathbf{\Lambda}$. In Fig. 7.3, we see two examples of such tissue samples. We stress that those samples do not need to have rectangular shape. Now, fix a sample $\mathbf{n}$ which is known to be normal to be the *reference normal*. For each one of the $\{\mathbf{s}_k\}_{k=1,2,\ldots,N}$, we derive the feature vector $f(\mathbf{s}_k; \mathbf{n})$ relative to $\mathbf{n}$ according to the following algorithm.

The first component of the feature vector $f(\mathbf{s}_k; \mathbf{n})$ is

$$D_M(\mathbf{s}_k, \mathbf{n}) := \frac{|\overline{\mathbf{s}}_k - \overline{\mathbf{n}}|}{\sqrt{var(\mathbf{s}_k) + var(\mathbf{n})}}.$$

D_M standardizes the statistical disparity due to the difference in the average attenuation intensity between $\mathbf{s}_k$ and $\mathbf{n}$. To form the remaining components of the feature vector $f(\mathbf{s}_k; \mathbf{n})$, we use the 3D rigid motion invariant statistical disparity $RD_j(\mathbf{s}_k, \mathbf{n})$ at scales $j = 0, -1$, between the 3D textures corresponding to $\mathbf{s}_k$ and $\mathbf{n}$ where

$$RD_j(\mathbf{s}_k, \mathbf{n}) = max\left\{0, \frac{Rdist_j(\mathbf{s}_k, \mathbf{n}) - diam_{\mathbf{n}}(j)}{diam_{\mathbf{n}}(j)}\right\}. \tag{7.13}$$

[16]. If for a given sample $\mathbf{s}_k$ and at some scale j, $RD_j(\mathbf{s}_k, \mathbf{n})$ is large, then we can conclude that the sample $\mathbf{s}_k$ has a different 3D texture than the reference normal $\mathbf{n}$ $\mathbf{s}_k$, thus more the tissue from which $\mathbf{s}_k$ originated is likely to be abnormal.

BOX 7.1   Algorithm for Computation of $RD_j(\mathbf{s}_k, \mathbf{n})$

   (i)   Adjust intensity values in both $\mathbf{s}_k$ and $\mathbf{n}$ to have zero mean.
   (ii) Upsample each $\mathbf{s}_k$ to a twice the denser grid as in [14], to approximate each $\mathbf{s}_k$ at a finer scale. The upsampled 3D texture sample is convolved with the isotropic low-pass synthe-

sis filter $\widehat{h}_0$:

$$\widehat{h}_0(\boldsymbol{\omega}) = \begin{cases} 1 & |\boldsymbol{\omega}| \leq \frac{1-b}{2t}, \\ \frac{1}{2}\left[1 + \cos\left(\frac{\pi t}{b}\left(|\boldsymbol{\omega}| - \frac{1-b}{2t}\right)\right)\right] & \frac{1-b}{2t} < |\boldsymbol{\omega}| \leq \frac{1+b}{2t}, \\ 0 & \text{otherwise}, \end{cases}$$

where $t = 100/84$ and $b = 1/7$. Repeat the process as needed (we upscale twice).

(iii) Let $\boldsymbol{\tau}$ be a node in $\mathbf{s}_k$, then a *neighborhood* of $\boldsymbol{\tau}$ is $\eta_{\boldsymbol{\tau}} := (\boldsymbol{\tau} + W) \subset \Lambda_k$ where W is a symmetric neighborhood of the origin. We set $W = W^+ \cup W^-$ where $W^- = -W^+$ and $W^+ = \{(2^{-j+1}, 0, 0), (0, 2^{-j+1}, 0), (0, 0, 2^{-j+1})\}$. The order-one GMRF model limits interactions within W. Also define $\Lambda'_k \subset \Lambda_k$ to satisfy $(\eta_{\boldsymbol{\tau}} + W) \subset \Lambda_k$ for every $\boldsymbol{\tau} \in \Lambda'_k$. We extract our statistics from $\mathbf{s}_k|_{\Lambda'_k}$.

(iv) Compute the empirical autocovariance matrix ζ_0 of $\mathbf{s}_k|_{\Lambda'_k}$ via:

$$\zeta_0(\boldsymbol{\tau}) = \frac{1}{|\Lambda'_k|} \sum_{r \in \Lambda'_k} s_{k_r} s_{k_{r+\tau}}, \quad \text{for all } \boldsymbol{\tau} \text{ such that } \|\boldsymbol{\tau}\|_\infty \leq 2^{-j+2},$$

where $|\Lambda'_k|$ denotes the number of voxels in Λ'_k; ζ_0 is of size $(2^{-j+3}+1)^3$.

(v) Any of the 3D textures need not satisfy $\zeta_0(\boldsymbol{\tau}) = \zeta_0(-\boldsymbol{\tau})$. So, we artificially symmetrize ζ'_0 by setting $\zeta'_0(\boldsymbol{\tau}) := \frac{1}{2}\left[\zeta_0(\boldsymbol{\tau}) + \zeta_0(-\boldsymbol{\tau})\right]$ for all $\boldsymbol{\tau} \in \Lambda'_k$ such that $\|\boldsymbol{\tau}\|_\infty \leq 2^{-j+2}$. To simplify the notation from now on, we use $\zeta'_0 = \zeta_0$.

(vi) Let $\mathbf{y}_r = [s_{k_l} + s_{k_{-l}}], l \in (r + W^+)$. Define $\mathbf{Y} = [\mathbf{y}_r], r \in \Lambda'_k$. The least squares estimates $\widehat{\sigma}$ and $\widehat{\beta}$ of the order-one GMRF model that fits the data are given by the statistics: $\widehat{\beta}(\mathbf{s}_k) = (\mathbf{Y}^T\mathbf{Y})^{-1}\mathbf{Y}^T\mathbf{s}_k$ and $\widehat{\sigma^2}(\mathbf{s}_k) = \frac{1}{|\Lambda'_k|}\left(\mathbf{s}_k^T\mathbf{s}_k - \widehat{\beta}^T\mathbf{Y}^T\mathbf{s}_k\right)$.

(vii) $\mathbf{Y}^T\mathbf{s}_k$ and $\mathbf{Y}^T\mathbf{Y}$ are given by $(\mathbf{Y}^T\mathbf{s}_k)_r = |\Lambda'_k|(\zeta_0(r) + \zeta_0(-r)) \;\; \forall r \in W^+$

$$(\mathbf{Y}^T\mathbf{Y})_{(\boldsymbol{\tau},r)} = |\Lambda'_k|[\zeta_0(r - \boldsymbol{\tau}) + \zeta_0(r + \boldsymbol{\tau}) + \zeta_0(-r - \boldsymbol{\tau}) + \zeta_0(-r + \boldsymbol{\tau})] \;(\boldsymbol{\tau}, r) \in W^+ \times W^+.$$

(viii) The computation of $(\mathbf{Y}^T\mathbf{Y})^{-1}$ is performed as in [14], using a least square solver.

(ix) Take a finite set of 3D rotations $\mathbf{A}_{(i,l,k)}$, over a grid $EB = [0, \pi] \times \left[0, \frac{\pi}{2}\right] \times [0, \pi]$, that is uniform with respect to Haar measure. Find rotations of ζ_0 on this grid to obtain $\zeta_0^{\mathbf{A}}$ for each i, l, k, using bilinear interpolation. It is important to avoid *gimbal lock* by choosing the grid points as prescribed in Section 7.4.

(x) $\Gamma_{\mathbf{X}}(\mathbf{A}) = (\widehat{\Sigma})_{\mathbf{A}}, \mathbf{A} \in SO(3)$. Hence order-one GMRF model parameters fitted on the rotated textures $\mathbf{s}_k^{\mathbf{A}}$ and $\mathbf{n}^{\mathbf{A}}$, is estimated by the correspondingly autocovariance matrix $\zeta_0^{\mathbf{A}}$ using the corresponding rotations by $\mathbf{A}$ of both $\mathbf{s}_k$ and $\mathbf{n}$.

(xi) Compute $Rdist_j(\mathbf{s}_k, \mathbf{n})$ by minimizing $F(v)$ over $v \in EB$, using a pattern search algorithm [79], where $F(v)$ is given by

$$F(v) = \frac{1}{N^3} \sum_{i=0}^{N-1} \sum_{l=0}^{N-1} \sum_{k=0}^{N-1} \text{KLdist}_j\left(\Gamma_{\mathbf{s}_k}(\mathbf{A}_{(i,l,k)}), \Gamma_{\mathbf{n}}(v\mathbf{A}_{(i,l,k)})\right).$$

> A computationally efficient way to compute KLdist is described in [14].
>
> **(xii)** Finally, $RD_j(\mathbf{s}_k, \mathbf{n})$ is computed for $j = 0, -1$ using the isotropic low-pass filter [16] with $t = \frac{2^{-j} \cdot 100}{84}$. We keep the low-pass output at the original resolution. To extract the order-one GMRF statistics, we use the interactions of pixels 2^{-j+1} apart and we repeat all of the previous steps with the exception of step (ii).

As noted in [16], the fitting of the same order–one GMRF model on decomposition of the same discrete texture at more than one scale, allows to incorporate texture information in the discriminative features from voxels that are not order-one neighbors. For classification we used SVMs, but it would be interesting to use a neural network with hidden layers.

7.7 CONCLUSION

In this chapter, we aimed to summarize various methods for the analysis of 3D textures with applications in biomedical imaging. We highlighted one particular method, which extracts second–order Gaussian features at multiple scales and average local intensities to generate an ensemble of discriminative features suitable for soft-tissue discrimination. The proposed features can be used with any binary classifier or even neural networks. The results and the details of the process of the experimental verification of the discriminability of the proposed features can be found in [16,80,15].

Our experiments only establish the capability of the proposed features for soft-tissue discrimination. Samples of tissue ROIs used for our experiments can be seen in Fig. 7.4. We do not claim that our method for hepatic tumor detection is a method that has been evaluated beyond the proof-of-concept stage. Experiments with synthetic textures, artificially rotated, show that combining the disparities between textures at different scales lead to rigid motion invariant classification of textures with high accuracy [16]. Experiments conducted with ROIs taken from gall bladder and muscle regions indicate that the textural disparity function has the capability of identifying tissue types that are significantly different, for instance, two organs or diseased from healthy tissue in contrast-enhanced X–ray CT scans [15]. We noticed that the rotational covariance of our features improves the clustering of normal tissues (Fig. 7.5) and that discrimination improves with the use of the local average disparity component D_M. On the other hand, for X–ray CT, D_M alone, is not sufficient for discrimination, while the vector of the textural disparities at various scales works better than D_M alone [15]. Furthermore, we wish to emphasize that stochastic textures often have statistical directional characteristics (*e.g.*, the eigendirections of the autocovariance matrix), which may not always be discernible by (convolutional) directional filters. The rotational covariance the IMRA filters improves the consistency of the extraction of these characteristics independently of the texture patch orientation (see evidence of this in Fig. 7.5 and in the results of
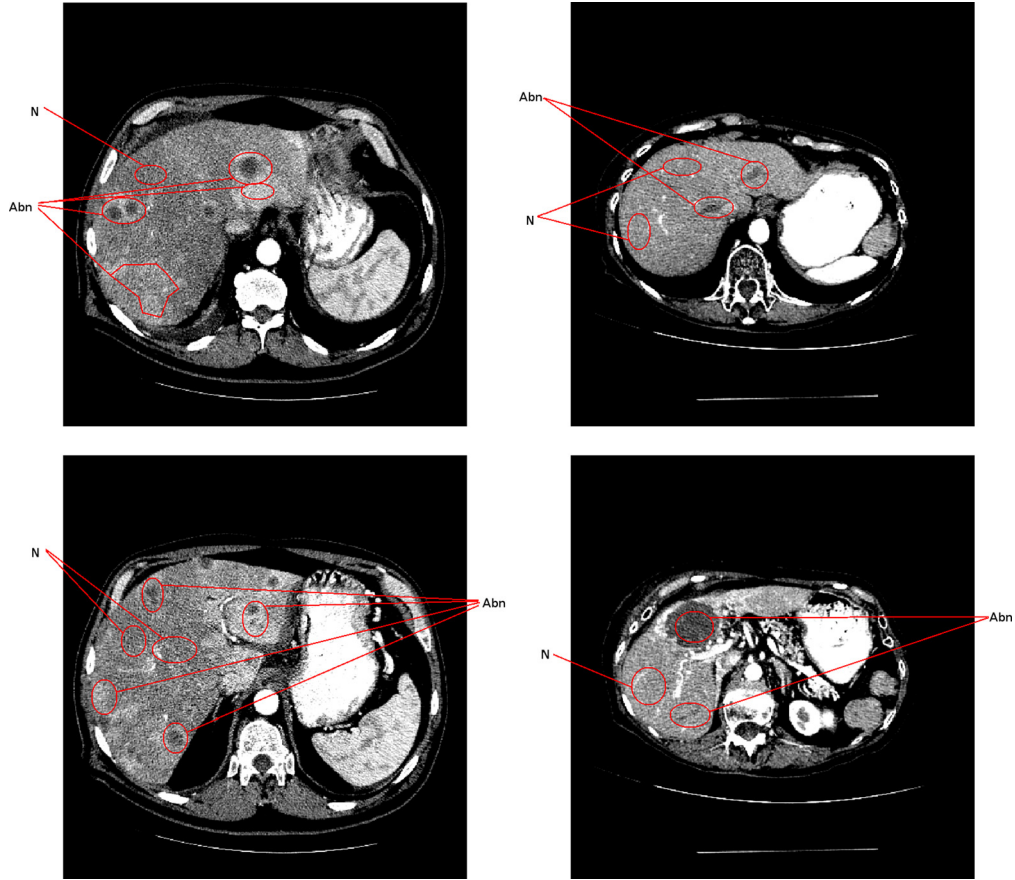
Figure 7.4 Examples of our choices of normal (N) and diseased (Abn) regions, whose cross-sections are shown in the above 2D slices. We selected many different kind of abnormalities for our experiments, which includes tumors of different sizes and from different stages

simulated texture experiments in [16]). To the best of our knowledge, there is no systematic study on how directional representations, *e.g.*, those listed in Section 2.4.2 of Chapter 2, affect the extraction of statistical directional characteristics of a stochastic texture when its orientation varies.

We have not examined how the method works with MRI or other modalities. However, the method is sufficiently broad to be customizable for other modalities.

Since the pathways for propagation can be absolutely random, we cannot expect the textures corresponding to cancerous ROIs to show any similarity. However, the normal regions of the same soft tissue type must be relatively similar to one another (see Fig. 7.4). So, the method we proposed can be utilized as an one-class classification method, where the proposed feature vectors from normal tissue will cluster, thus their
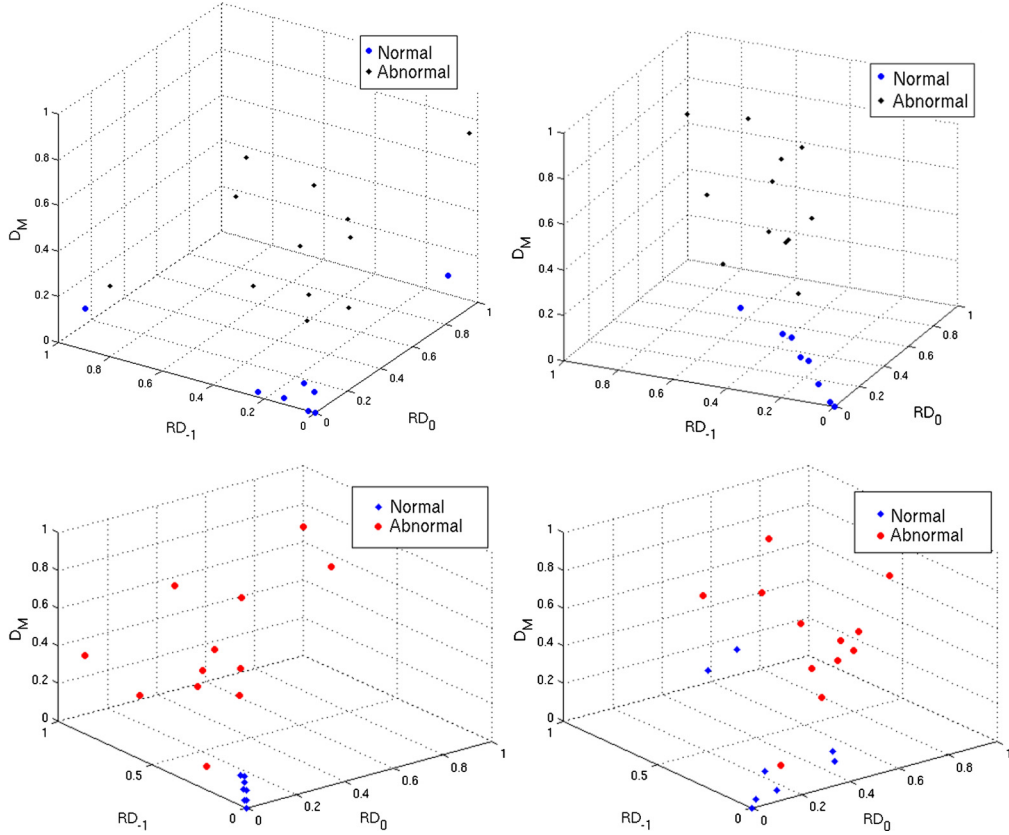
Figure 7.5 Scatterplots show that the use of 3D rotationally invariant texture disparities improves normal tissue ROI feature vector clustering. Left: RD_j's given by texture distance $Rdist_j$ (Eq. (7.11)). Most feature vectors from normal tissue ROIs cluster around the origin and clearly away from their abnormal ROI counterparts. Right: texture disparities are computed using $KLdist$ only, without averaging over 3D rotations. The normal tissue ROI cluster is less pronounced and is more proximal to abnormal tissue ROI feature vectors.

disparities will be smaller than those of abnormal regions. Clearly, what we propose is a system for screening ROIs, as if one is looking with a torchlight, and not a diagnostic system. Once an ROI is flagged, an expert will have to inspect it and render a diagnosis. Our method has the ability to combine the classical approach based on the different attenuation values resulting from tissue variation, which is what all radiologists have been trained to look for, but also 3D features which exploit the full power of the 3D information modern scanners provide.

Since we proposed this method a number of other approaches aiming to incorporate rotational invariance in the classification have been developed, exploiting the power of directional filters. However, directional filters are not compactly supported in the space

domain and do not provide full rotational invariance, in their discrete implementations. On the other hand, IMRA filters offer full rotational invariance to the resulting statistical disparities, but the numerical implementation of these disparities makes this invariant only approximate. KL-distances are computed via numerically implemented integrations. Also IMRA filters are themselves not compactly supported in space as Theorem 7.2 shows. Having all of these limitations in mind, we proposed in Section 7.3 a method to, at least, use finite length filters in 2D or 3D to avoid ringing in order to extract the approximations of the rotations of each s_k.

REFERENCES

[1] F.S. Cohen, Z. Fan, M.A. Patel, Classification of rotated and scaled textured images using Gaussian Markov Random Field models, IEEE Trans. Pattern Anal. Mach. Intell. 13 (2) (1991) 192–202.

[2] R. Haralick, Statistical and structural approaches to texture, Proc. IEEE 67 (5) (1979) 610–621.

[3] S.Y. Lu, K.S. Fu, A syntactic approach to texture analysis, Comput. Graph. Image Process. 7 (1978) 303–330.

[4] R. Chin, C. Harlow, Automated visual inspection: a survey, IEEE Trans. Pattern Anal. Mach. Intell. PAMI-4 (6) (1982) 557–573.

[5] F. Tomita, S. Tsuji, Computer Analysis of Visual Textures, Kluwer Academic Publishers, 1990.

[6] P. Cirujeda, Y.D. Cid, H. Müller, D. Rubin, T.A. Aguilera, B.W. Loo, M. Diehn, X. Binefa, A. Depeursinge, A 3-D Riesz-covariance texture model for prediction of nodule recurrence in lung CT, IEEE Trans. Med. Imaging 35 (12) (Dec 2016) 2620–2630.

[7] A. Depeursinge, A. Foncubierta-Rodriguez, D. Van de Ville, H. Müller, Multiscale Lung Texture Signature Learning Using the Riesz Transform, Springer, Berlin, Heidelberg, 2012, pp. 517–524.

[8] A. Depeursinge, A. Foncubierta-Rodriguez, D. Van de Ville, H. Müller, Rotation-covariant texture learning using steerable Riesz wavelets, IEEE Trans. Image Process. 23 (2) (Feb 2014) 898–908.

[9] F. Orlhac, C. Nioche, M. Soussan, I. Buvat, Understanding changes in tumor textural indices in pet: a comparison between visual assessment and index values in simulated and patient data, J. Nucl. Med. (2016).

[10] A. Kassner, R.E. Thornhill, Texture analysis: a review of neurologic MR imaging applications, Am. J. Neuroradiol. 31 (5) (2010) 809–816.

[11] A. Depeursinge, A. Foncubierta-Rodríguez, A. Vargas, D. Van de Villey, A. Platon, P.-A. Poletti, H. Müller, Rotation-covariant texture analysis of 4D dual-energy CT as an indicator of local pulmonary perfusion, in: 2013 IEEE 10th International Symposium on Biomedical Imaging (ISBI), IEEE, 2013, pp. 145–148.

[12] A. Depeursinge, A. Foncubierta-Rodriguez, D. Van De Ville, H. Müller, Three-dimensional solid texture analysis in biomedical imaging: review and opportunities, Med. Image Anal. 18 (January 2014) 176–196.

[13] I.M. Elfadel, R.W. Picard, Gibbs random fields, cooccurrences, and texture modeling, IEEE Trans. Pattern Anal. Mach. Intell. 16 (1) (1994) 24–37.

[14] S. Upadhyay, S. Jain, M. Papadakis, R. Azencott, 3D-rigid motion invariant discrimination and classification of 3D-textures, Proc. SPIE 8138 (2011) 813821.

[15] S. Upadhyay, M. Papadakis, S. Jain, G.W. Gladish, I.A. Kakadiaris, R. Azencott, Semi-automatic discrimination of normal tissue and liver cancer lesions in contrast enhanced X-ray CT-scans, in: H. Yoshida, D. Hawkes, M. Vannier (Eds.), Proc. Computational and Clinical Applications in Abdominal Imaging, Nice, France, vol. 7601, Springer, October 1–5, 2012, pp. 158–167.

[16] S. Jain, M. Papadakis, S. Upadhyay, R. Azencott, Rigid motion invariant classification of 3D-textures, IEEE Trans. Image Process. 21 (5) (May 2012) 2449–2463.

[17] R. Porter, N. Canagarajah, Robust rotation-invariant texture classification: wavelet, Gabor filter and GMRF based schemes, IEE Proc., Vis. Image Signal Process. 144 (3) (1997) 180–188.

[18] A. Teuner, O. Pichler, B.J. Hosticka, Unsupervised texture segmentation of images using tuned Gabor filters, IEEE Trans. Image Process. 4 (6) (1995) 863–870.

[19] R. Azencott, J.P. Wang, L. Younes, Texture classification using Gabor filters, IEEE Trans. Pattern Anal. Mach. Intell. 19 (2) (1997) 148–152.

[20] D. Dunn, W.E. Higgins, Optimal Gabor filters for texture segmentation, IEEE Trans. Pattern Anal. Mach. Intell. 16 (1994) 947–964.

[21] T.S. Lee, Image representation using 2D Gabor wavelets, IEEE Trans. Pattern Anal. Mach. Intell. 18 (1996) 959–971.

[22] K. Etemad, R. Chellappa, Separability based tree-structured local basis selection for texture classification, in: ICIP 1994, vol. 3, Austin, TX, 1994.

[23] T. Chang, C. Kuo, Texture analysis and classification with tree-structured wavelet transform, IEEE Trans. Image Process. 2 (4) (1995) 429–441.

[24] M. Unser, Texture classification and segmentation using wavelet frames, IEEE Trans. Image Process. 2 (4) (1995) 429–441.

[25] M. Do, M. Vetterli, Rotation invariant texture characterizaton and retrieval using steerable wavelet domain hidden Markov models, IEEE Trans. Multimed. 4 (4) (2002) 517–527.

[26] H. Choi, R. Baraniuk, Multiscale image segmentation using wavelet domain hidden Markov models, in: Conf. Mathem. Model., Bayes Est., Inv. Prob., Proc. SPIE 3816 (1999) 306–320.

[27] S.K. Alexander, R. Azencott, M. Papadakis, Isotropic multiresolution analysis for 3D-textures and applications in cardiovascular imaging, in: D. Van Der Ville, V. Goyal, M. Papadakis (Eds.), Wavelets XII, Proc. SPIE 6701 (2007) 67011S.

[28] R.L. Kashyap, Analysis and synthesis of image patterns by spatial interaction models, in: Progress in Pattern Recognition, 1981, pp. 149–186.

[29] R. Chellappa, Two-dimensional discrete Gaussian Markov random field models for image processing, in: Progress in Pattern Recognition, vol. 2, 1985, pp. 79–112.

[30] J. Mao, A.K. Jain, Texture classification and segmentation using multiresolution simultaneous autoregressive models, Pattern Recognit. 25 (2) (1992) 173–188.

[31] G.R. Cross, A.K. Jain, Markov random field texture models, IEEE Trans. Pattern Anal. Mach. Intell. PAMI (5) (1983) 25–39.

[32] C. Bouman, B. Liu, Multiple resolution segmentation of textured images, IEEE Trans. Pattern Anal. Mach. Intell. PAMI-13 (2) (1991) 99–113.

[33] R. Azencott, C. Graffigne, C. Labourdette, Edge detection and segmentation of textured images using Markov fields, in: Lecture Notes in Statistics, vol. 74, Springer-Verlag, 1992, pp. 75–88.

[34] S. Geman, D. Geman, Stochastic relaxation, Gibbs distributions, and the Bayesian restoration of images, IEEE Trans. Pattern Anal. Mach. Intell. 6 (1984) 721–741.

[35] H. Derin, H. Elliott, Modeling and segmentation of noisy and textured images using Gibbs random fields, IEEE Trans. Pattern Anal. Mach. Intell. PAMI-9 (1) (1987) 39–55.

[36] R.L. Kashyap, R. Chellappa, Estimation and choice of neighbors in spatial-interaction models of images, IEEE Trans. Inf. Theory 1 (1983) 60–72.

[37] E. Boykova Ranguelova, Segmentation of Textured Images on Three-Dimensional Lattices, PhD Thesis, University of Dublin, Trinity College, 2002.

[38] V.A. Kovalev, F. Kruggel, H.J. Gertz, D.Y. von Cramon, Three-dimensional texture analysis of MRI brain datasets, IEEE Trans. Med. Imaging 20 (5) (2001) 424–433.

[39] A.S. Kurani, D.H. Xu, J.D. Furst, D.S. Raicu, Co-occurrence matrices for volumetric data, in: 7th IASTED International Conference on Computer Graphics and Imaging, 2004.

[40] D.H. Xu, A.S. Kurani, J.D. Furst, D.S. Raicu, Run-length encoding for volumetric texture, in: 4th IASTED International Conference on Visualization, Imaging and Image Processing, 2004.

[41] A. Madabhushi, M. Feldman, D. Metaxas, D. Chute, J. Tomaszewski, A novel stochastic combination of 3D texture features for automated segmentation of prostatic adenocarcinoma from high resolution MRI, in: Medical Image Computing and Computer-Assisted Intervention, vol. 2878, 2003, pp. 581–591.

[42] C.C. Reyes-Aldasoro, A. Bhalerao, Volumetric feature selection for MRI, Inf. Process. Med. Imag. 2732 (2003) 282–293.

[43] D. Pescia, N. Paragios, S. Chemouny, Automatic detection of liver tumors, in: 5th IEEE International Symposium on Biomedical Imaging: From Nano to Macro, May 2008, pp. 672–675.

[44] R.M. Haralick, K. Shanmugam, I. Dinstein, Textural features for image classification, IEEE Trans. Syst. Man Cybern. 3 (1973) 610–621.

[45] J. Liu, Q. Hu, Z. Chen, P. Heng, Adaptive liver segmentation from multi-slice CT scans, in: Y. Peng, X. Weng (Eds.), 7th Asian-Pacific Conference on Medical and Biological Engineering, in: Proc. IFMBE Proceedings, vol. 19, Springer, 2008, pp. 381–384.

[46] R. Susomboon, D. Raicu, J. Furst, T.B. Johnson, A co-occurrence texture semi-invariance to direction, distance and patient size, in: J.M. Reinhardt, J.P.W. Pluim (Eds.), Proc. Medical Imaging 2008: Image Processing, Proc. SPIE 6914 (2008).

[47] M. Pham, R. Susomboon, T. Disney, D. Raicu, J. Furst, A comparison of texture models for automatic liver segmentation, in: J.P.W. Pluim, J.M. Reinhardt (Eds.), Proc. Medical Imaging 2007: Image Processing, Proc. SPIE 6512 (2007).

[48] N.H. Abdel-massieh, M.M. Hadhoud, K.M. Amin, Automatic liver tumor segmentation from CT scans with knowledge-based constraints, in: Proc. Biomedical Engineering Conference (CIBEC), 2010 5th Cairo International, Cairo International Biomedical Engineering Conference, IEEE, December 2010, pp. 215–218.

[49] A. Militzer, T. Hager, F. Jager, C. Tietjen, J. Hornegger, Automatic detection and segmentation of focal liver lesions in contrast enhanced CT images, in: 2010 20th International Conference on Proc. Pattern Recognition (ICPR), IEEE, August 2010, pp. 2524–2527.

[50] L. Massoptier, S. Casciaro, A new fully automatic and robust algorithm for fast segmentation of liver tissue and tumors from CT scans, Eur. Radiol. 18 (8) (2008) 1658–1665, http://dx.doi.org/10.1007/s00330-008-0924-y.

[51] Z.H. Zhou, X.Y. Liu, On multi-class cost-sensitive learning, Comput. Intell. 26 (3) (August 2010) 232–257.

[52] K.S. Seo, Automatic hepatic tumor segmentation using composite hypothesis, in: Second International Conference on Image Analysis and Recognition (ICIAR '05), in: Proc. Lecture Notes in Computer Science, vol. 3656, Springer, 2005.

[53] S.J. Park, K.S. Seo, J.A. Park, Automatic hepatic tumor segmentation using statistical optimal threshold, in: V. Sunderam, G. van Albada, P. Sloot, J. Dongarra (Eds.), 5th International Conference On Computational Science (ICCS '05), in: Proc. Lecture Notes in Computer Science, vol. 3514, 2005.

[54] M.P. Jolly, L. Grady, 3D general lesion segmentation in CT, in: Proc. Biomedical Imaging: From Nano to Macro. 5th IEEE International Symposium on Biomedical Imaging, IEEE, 2008.

[55] T. Chen, D. Metaxas, A hybrid framework for 3D medical image segmentation, Med. Image Anal. 9 (6) (2005) 547–565.

[56] I. Daubechies, Ten Lectures on Wavelets, CBMS, vol. 61, SIAM, 1992.

[57] J.R. Romero, S.K. Alexander, S. Baid, S. Jain, M. Papadakis, The geometry and the analytic properties of isotropic multiresolution analysis, Adv. Comput. Math. 31 (1) (2009) 283–328.

[58] E.H. Adelson, E. Simoncelli, R. Hingoranp, Orthogonal pyramid transforms for image coding, in: Visual Communications and Image Processing II, Proc. SPIE 845 (1987) 50–58.

[59] E.P. Simoncelli, W.T. Freeman, E.H. Adelson, D.J. Heeger, Shiftable multi-scale transforms, IEEE Trans. Inf. Theory 38 (2) (1992) 587–607.

[60] A. Karasaridis, E. Simoncelli, A filter design technique for steerable pyramid image transforms, in: Acoustics Speech and Signal Processing, ICASP, Atlanta, GA, May 7–10 1996.

[61] W.T. Freeman, E.H. Adelson, The design and use of steerable filters, IEEE Trans. Pattern Anal. Mach. Intell. 13 (9) (1991) 891–906.

[62] J. Portilla, V. Strela, M.J. Wainwright, E.P. Simoncelli, Image denoising using Gaussian scale mixtures in the wavelet domain, IEEE Trans. Image Process. 12 (2003) 1338–1351, Computer Science techn. rep. nr. TR2002-831, Courant Institute of Mathematical Sciences.

[63] J.M. Coggins, A.K. Jain, A spatial filtering approach to texture analysis, Pattern Recognit. Lett. 3 (3) (1985) 195–203.

[64] A.K. Jain, F. Farrokhnia, Unsupervised texture segmentation using Gabor filters, IEEE Trans. Pattern Anal. Mach. Intell. 18 (2) (1991) 1167–1186.

[65] P. Heinlein, J. Drexl, W. Schneider, Integrated wavelets for enhancement of microcalcifications in digital mamography, IEEE Trans. Med. Imaging 22 (3) (2003) 402–413.

[66] G. Tzagkarakis, B. Beferull-Lozano, P. Tsakalides, Rotation-invariant texture retrieval with Gaussianized steerable pyramids, IEEE Trans. Image Process. 15 (9) (2006) 2702–2718.

[67] Y. Wan, R.D. Nowak, Quasi-circular rotation invariance in image denoising, in: ICIP, vol. 1, 1999, pp. 605–609.

[68] M. Unser, N. Chenouard, A unifying parametric framework for 2D steerable wavelet transforms, SIAM J. Imaging Sci. 6 (1) (2013) 102–135.

[69] N. Chenouard, M. Unser, 3D steerable wavelets in practice, IEEE Trans. Image Process. 21 (11) (2012) 4522–4533.

[70] M. Unser, N. Chenouard, D. Van De Ville, Steerable pyramids and tight wavelet frames in $l_2(\mathbb{R}^d)$, IEEE Trans. Image Process. 20 (10) (October 2011) 2705–2721.

[71] M. Papadakis, G. Gogoshin, I.A. Kakadiaris, D.J. Kouri, D.K. Hoffman, Non-separable radial frame multiresolution analysis in multidimensions, Numer. Funct. Anal. Optim. 24 (2003) 907–928.

[72] E. Hernández, G. Weiss, A First Course on Wavelets, CRC Press, Boca Raton, FL, 1996.

[73] S. Lakshmanan, H. Derin, Valid parameter space for 2-D Gaussian Markov Random Fields, IEEE Trans. Inf. Theory 39 (2) (1993) 703–709.

[74] R.L. Kashyap, A. Khotanazad, A model-based method for rotation invariant texture classification, IEEE Trans. Pattern Anal. Mach. Intell. 8 (4) (1986) 472–481.

[75] M. Papadakis, B.G. Bodmann, S.K. Alexander, D. Vela, S. Baid, A.A. Gittens, D.J. Kouri, S.D. Gertz, S. Jain, J.R. Romero, X. Li, P. Cherukuri, D.D. Cody, G.W. Gladish, I. Aboshady, J.L. Conyers, S.W. Casscells, Texture-based tissue characterization for high-resolution CT-scans of coronary arteries, Commun. Numer. Methods Eng. 25 (2009) 597–613.

[76] J. Fehr, H. Burkhardt, 3D rotation invariant local binary patterns, in: ICPR 2008, Tampa, FL, 2008.

[77] R. Azencott, D. Dacunha-Castelle, Series of Irregular Observations, Springer-Verlag, 1986.

[78] B.G. Bodmann, M. Papadakis, et al., Frame isotropic multiresolution analysis for micro CT scans of coronary arteries, in: M. Papadakis, A. Laine, M. Unser (Eds.), Wavelets XI, Proc. SPIE 5914 (2005) 59141O.

[79] C. Audet, J.E. Dennis Jr., Analysis of generalized pattern searches, SIAM J. Optim. 13 (3) (2002) 889–903.

[80] S. Upadhyay, S. Jain, M. Papadakis, R. Azencott, 3D-rigid motion invariant discrimination and classification of 3D-textures, in: M. Papadakis, D. Van De Ville, V. Goyal (Eds.), Wavelets and Sparsity XIV, Proc. SPIE 8138 (2011), http://dx.doi.org/10.1117/12.891721.